Open access • Journal Article • DOI:10.1016/J.COMPOSITESB.2017.09.043

Bending and buckling analyses of functionally graded polymer composite plates reinforced with graphene nanoplatelets — Source link

Mitao Song, Mitao Song, Jie Yang, Sritawat Kitipornchai

Institutions: Jiangsu University, University of Queensland, RMIT University

Published on: 01 Feb 2018 - Composites Part B-engineering (Elsevier)

Topics: Buckling and Micromechanics

Accepted Manuscript

Bending and buckling analyses of functionally graded polymer composite plates reinforced with graphene nanoplatelets

Mitao Song, Jie Yang, Sritawat Kitipornchai

PII: S1359-8368(16)32458-1

DOI: 10.1016/j.compositesb.2017.09.043

Reference: JCOMB 5290

To appear in: *Composites Part B*

Received Date: 26 October 2016

Accepted Date: 18 September 2017

Please cite this article as: Song M, Yang J, Kitipornchai S, Bending and buckling analyses of functionally graded polymer composite plates reinforced with graphene nanoplatelets, *Composites Part B* (2017), doi: 10.1016/j.compositesb.2017.09.043.

Bending and buckling analyses of functionally graded polymer composite plates reinforced with graphene nanoplatelets

Mitao Song [a, b], Jie Yang [c,*], Sritawat Kitipornchai [a]

[a] *School of Civil Engineering, The University of Queensland, St Lucia, Brisbane, QLD 4072, Australia*

[b] *Faculty of Civil Engineering and Mechanics, Jiangsu University, Zhenjiang, Jiangsu 212013, P.R. China*

[c] *School of Engineering, RMIT University, PO Box 71, Bundoora, VIC 3083, Australia*

Bending and buckling analyses of functionally graded polymer composite plates reinforced with graphene nanoplatelets

Mitao Song [a, b], Jie Yang [c,*], Sritawat Kitipornchai [a]

[a] *School of Civil Engineering, The University of Queensland, St Lucia, Brisbane, QLD 4072, Australia*

[b] *Faculty of Civil Engineering and Mechanics, Jiangsu University, Zhenjiang, Jiangsu 212013, P.R. China*

[c] *School of Engineering, RMIT University, PO Box 71, Bundoora, VIC 3083, Australia*

Abstract

This paper presents static bending and compressive buckling analyses of functionally graded multilayer graphene nanoplatelet (GPL)/polymer composite plates within the framework of the first-order shear deformation theory. The GPL weight fraction shows a layer-wise change along the thickness direction with GPLs uniformly dispersed in the polymer matrix in each individual layer. The effective Young's modulus of the nanocomposites is estimated through the Halpin-Tsai micromechanics model while the effective Poisson's ratio is determined by the rule of mixture. Analytical solutions are obtained for the static deflection and critical buckling load of the simply supported functionally graded GPL/polymer plates by using the Navier solution technique. Numerical results show that GPL distribution pattern, weight fraction, and geometry and size have significant influences on the bending and buckling behaviors of the functionally graded GPL reinforced nanocomposite plate.

Keywords: Graphene nanoplatelets; Functionally grade materials; Polymer composites; The first-order shear deformation plate theory; Bending; Buckling

---

[*] Corresponding author. Tel.: 61-03-99256169; Fax: 61-03-99256108

E-mail address: j.yang@rmit.edu.au (J. Yang)

1. Introduction

Graphene and its derivatives such as graphene nanoplatelets (GPLs) [1] are new two-dimensional carbon materials that have recently received considerable research attention because of their extraordinary mechanical [2], thermal [3, 4], and electrical properties [5]. Compared with carbon nanotubes (CNTs), they have a much bigger specific surface area which provides a much stronger bonding with the matrix hence the greatly enhanced load transfer capability. It has been theoretically and experimentally observed that the addition of a very small amount of GPLs into the pristine polymer matrix can dramatically improve its mechanical properties [6-10]. For instance, Rafiee et al. [6] demonstrated that by adding 0.1% weight fraction (wt.%) of GPLs, the strength and stiffness of the reinforced polymer composites are enhanced by the same degree achieved by adding 1.0 w.t.% of CNTs. The outstanding reinforcing effect and the relatively low manufacturing cost compared with that of single graphene sheet make GPLs excellent candidates as the reinforcement materials in developing advanced light weight composite structures [11].

The majority of the existing investigations in this emerging area are focused on the synthesis/ fabrication technique, and material property characterization of graphene based nanocomposites with low content of graphene nanofillers. Fang et al. [12] developed an efficient method to functionalize graphene nanosheets and manufactured polystyrene nanocomposites with the addition of 0.9 w.t.% graphene nanosheets and achieved around 70% and 57% increase in tensile strength and Young's modulus, respectively. By adding 1.8 wt.% of graphene oxide into poly (vinyl alcohol) (PVA) matrix and reducing graphene oxide into graphene nanosheets, Zhao et al. [13] fabricated graphene-reinforced PVA composite films with a 150% improvement in tensile strength and a nearly 10 times increase in Young's modulus. King et al. [14] manufactured nanocomposites containing 1.0~6.0 wt.% GPLs in epoxy and tested the tensile properties via macroscopic methods and nanoindentation. They found that the tensile modulus increases from 2.72 GPa for the pure epoxy to 3.36 GPa by embedding 6.0 wt.% GPLs in epoxy matrix. Wang et al. [15] dispersed GPLs with different sizes to epoxy resin using a sonication process followed by three-roll milling, and studied the effects of GPL sizes on the mechanical properties of

GPL/epoxy nanocomposites. Their study indicated that a larger GPL size can significantly improve the tensile modulus but reduce the strength of the nanocomposites. Among the theoretical and numerical studies on graphene based nanocomposites, Ji et al. [16] used Mori-Tanaka micromechanics method to investigate the effective elastic properties of nanocomposites reinforced by exfoliated graphene sheets. Their study showed that a very low content of graphene sheets can considerably enhance the effective stiffness of the composite and also verified that graphene sheets outperform CNTs as reinforcement nanofillers. Rahman and Haque [17] investigated the mechanical properties of graphene/epoxy nanocomposites using molecular mechanics and molecular dynamics simulations, and observed that dispersing graphene with a high aspect ratio provides improved in-plane Young's modulus of graphene/epoxy nanocomposites in comparison to agglomerated graphene system. Montazeri and Rafii-Tabar [10] employed a molecular structural mechanics/finite element-based multiscale modeling approach to compute the elastic constants of a polymeric nanocomposite embedded with graphene sheets. They found that the presence of ripples on the surface of the embedded graphene sheets decreases the axial Young modulus of the nanocomposites. Spanos et al. [18] estimated the elastic mechanical properties of graphene reinforced composites by using a multiscale finite element method in which the graphene is modeled based on its atomistic microstructure while the matrix is modeled by continuum finite element method.

Structural analysis of carbon-based composite structures is very important in the successful design and applications of this novel nanocomposites. The static bending, elastic buckling, postbuckling, free and forced vibrations, bifurcation and chaotic movement of CNTs reinforced composite structures have been extensively investigated [19-26]. Studies on the structural behavior of graphene reinforced composite structures, however, is quite limited. Chandra et al. [27] proposed a multiscale finite element method for the natural frequencies and mode shapes of graphene/polymer composite structures by modeling graphene and polymer matrix with the atomistic and conventional continuum finite element methods, respectively. Cranford [28] used a hybrid full atomistic and coarse-grained molecular dynamics approach to study the buckling

induced delamination of mono- and bilayer graphene-based composites. Rissanou et al. [29] studied the structural and dynamical properties of several graphene based polymer nanocomposites with graphene sheets of different sizes but at the same concentration through atomistic molecular dynamic simulations. It should be noted that previous studies were focused on the nanocomposites reinforced with mono- or multilayer graphene layers or uniformly dispersed graphene sheets only. Most recently, Song et al. [30] investigated the linear free and forced vibrations of functionally graded polymer nanocomposite plates in which GPLs are non-uniformly dispersed in the matrix. Their study found that the way GPLs are distributed plays an important role in the mechanical performance of the nanocomposite structure and a functionally graded non-uniform GPL distribution pattern, if appropriately chosen, offers much better reinforcing effect than the commonly used uniform distribution.

Motivated by this important observation, the objective of the present paper is to further investigate the bending and buckling behaviors of functionally graded GPL/polymer nanocomposite plates. Since it is extremely difficult to fabricate an ideal functionally grade plate with GPL concentration varying continuously due to the constraint of the current manufacturing technology, a multilayer plate structure in which GPLs are uniformly dispersed within each individual layer but its weight fraction shows a layer-wise gradual change along plate thickness, are considered instead. Such a structure can easily get rid of the great difficulty in material fabrication yet represents an excellent alternative for the ideal functionally graded structure if the total number of layers is sufficiently large. The micromechanics based Halpin-Tsai model is employed to predict the effective Young's modulus while the rule of mixture is used to determine the effective Poisson's ratio. Theoretical formulations are based on the first-order shear deformation plate theory. Navier solution technique is used to obtain the static deflection and the critical buckling load of a simply supported nanocomposite plate. A detailed parametric study is then carried out to highlight the effects of the distribution pattern, weight fraction, geometry and size of GPLs as well as the total number of layers on the bending deflection and critical buckling load of the functionally graded GPL/polymer nanocomposite plate.

2. Problem Formulation

Fig. 1 shows a multilayer GPL/polymer nanocomposite plate with length a, width b, thickness h and subjected to a transverse static load $F(X, Y)$ and in-plane compressive loads $\bar{N}_x^0$ along the X-axis and $\bar{N}_y^0$ along the Y-axis. The plate consists of N_L individual layers with the same thickness h / N_L. It is assumed that GPLs act as effective rectangular solid fillers uniformly dispersed in the polymer matrix of each layer. The GPL weight fraction changes from layer to layer along the thickness direction to form a functionally graded structure. Four types of GPL distribution patterns as shown in Fig. 2 are considered where the uniform and the other three non-uniform GPL distribution patterns are denoted by UD, FG-O, FG-X, and FG-A, respectively. The mid-plane of the plate is GPL rich in FG-O while both the top and bottom surfaces are GPL rich in FG-X. It should be noted that UD is a special case corresponding to an isotropic homogeneous plate and that all patterns are symmetric except for FG-A, in which GPL weight fraction increases monotonically from the top surface to the bottom surface.

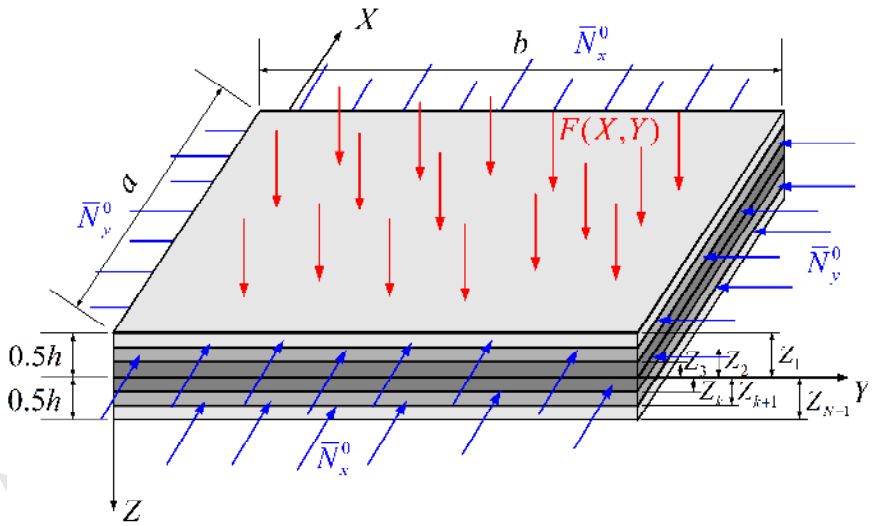

Fig. 1. A laminated graphene platelet (GPL)/polymer composite plate

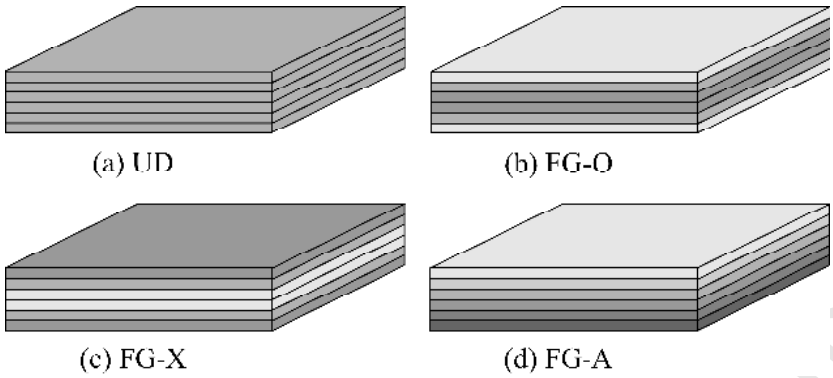

Fig. 2. Schematic diagrams of four GPL distribution patterns in the multilayer GPL/polymer nanocomposite plate

The effective Young's modulus of the GPL/polymer nanocomposite, E_{C}, can be predicated by Halpin-Tsai micromechanics model [30]:

$$E_{\mathrm{C}} = \frac{3}{8}\frac{1+\xi_{\mathrm{L}}\eta_{\mathrm{L}}V_{\mathrm{GPL}}}{1-\eta_{\mathrm{L}}V_{\mathrm{GPL}}}\times E_{\mathrm{M}} + \frac{5}{8}\frac{1+\xi_{\mathrm{W}}\eta_{\mathrm{W}}V_{\mathrm{GPL}}}{1-\eta_{\mathrm{W}}V_{\mathrm{GPL}}}\times E_{\mathrm{M}} \tag{1}$$

$$\eta_{\mathrm{L}} = \frac{(E_{\mathrm{GPL}}/E_{\mathrm{M}})-1}{(E_{\mathrm{GPL}}/E_{\mathrm{M}})+\xi_{\mathrm{L}}} \tag{2}$$

$$\eta_{\mathrm{W}} = \frac{(E_{\mathrm{GPL}}/E_{\mathrm{M}})-1}{(E_{\mathrm{GPL}}/E_{\mathrm{M}})+\xi_{\mathrm{W}}} \tag{3}$$

where E_{M} and E_{GPL} are Young's moduli of the polymer matrix and GPLs, respectively. ξ_{L} and ξ_{W} are the parameters characterizing both the geometry and size of GPL naofillers, defined as

$$\xi_{\mathrm{L}} = 2\left(\frac{l_{\mathrm{GPL}}}{h_{\mathrm{GPL}}}\right), \quad \xi_{\mathrm{W}} = 2\left(\frac{w_{\mathrm{GPL}}}{h_{\mathrm{GPL}}}\right) \tag{4}$$

in which l_{GPL}, w_{GPL} and h_{GPL} are the average length, width, and thickness of the GPLs whose volume fraction V_{GPL} is given by

$$V_{\mathrm{GPL}} = \frac{g_{\mathrm{GPL}}}{g_{\mathrm{GPL}} + (\rho_{\mathrm{GPL}}/\rho_{\mathrm{M}})(1-g_{\mathrm{GPL}})} \tag{5}$$

where g_{GPL} is GPL weight fraction in the nanocomposite, and ρ_{M} and ρ_{GPL} are the mass

densities of polymer matrix and GPLs, respectively.

According to the rule of mixture, the effective Possion's ratio ν_C of the GPL/ polymer nanocomposite can be calculated by way of

$$\nu_C = \nu_{GPL} V_{GPL} + \nu_M V_M \tag{6}$$

where V_M is the volume fraction of polymer matrix, ν_M and ν_{GPL} are Possion's ratios of polymer matrix and GPLs, respectively.

Based on the first-order shear deformation plate theory, the displacement fields at a point in the plate can be expressed as [31]

$$\begin{Bmatrix} \bar{U}(X,Y,Z) \\ \bar{V}(X,Y,Z) \\ \bar{W}(X,Y,Z) \end{Bmatrix} = \begin{Bmatrix} U(X,Y) \\ V(X,Y) \\ W(X,Y) \end{Bmatrix} + Z \begin{Bmatrix} \Psi_x(X,Y) \\ \Psi_y(X,Y) \\ 0 \end{Bmatrix} \tag{7}$$

where $U(X,Y)$, $V(X,Y)$ and $W(X,Y)$ are the displacement components at a point on the mid-plane of the plate, Ψ_x and Ψ_y represent the rotations of the *X*-*Z* and *Y*-*Z* planes, respectively.

According to the Hamilton's principle, the governing differential equations can be obtained in terms of stress resultants and moment resultants as follows:

$$\frac{\partial H_x}{\partial X} + \frac{\partial H_{xy}}{\partial Y} = 0 \tag{8}$$

$$\frac{\partial H_{xy}}{\partial X} + \frac{\partial H_y}{\partial Y} = 0 \tag{9}$$

$$\frac{\partial Q_x}{\partial X} + \frac{\partial Q_y}{\partial Y} + \bar{N} + F(X,Y) = 0 \tag{10}$$

$$\frac{\partial M_x}{\partial X} + \frac{\partial M_{xy}}{\partial Y} - Q_x = 0 \tag{11}$$

$$\frac{\partial M_{xy}}{\partial X} + \frac{\partial M_y}{\partial Y} - Q_y = 0 \tag{12}$$

where $\bar{N} = \bar{N}_x^0 \frac{\partial^2 W}{\partial X^2} + 2\bar{N}_{xy}^0 \frac{\partial^2 W}{\partial X \partial Y} + \bar{N}_y^0 \frac{\partial^2 W}{\partial Y^2}$. The stress resultants, moment resultants and shear

forces are related to strain components by:

$$\begin{Bmatrix} H_x \\ H_y \\ H_{xy} \end{Bmatrix} = \left[\bar{A}\right] \begin{Bmatrix} \varepsilon_x^{(0)} \\ \varepsilon_y^{(0)} \\ \gamma_{xy}^{(0)} \end{Bmatrix} + \left[\bar{B}\right] \begin{Bmatrix} \varepsilon_x^{(1)} \\ \varepsilon_y^{(1)} \\ \gamma_{xy}^{(1)} \end{Bmatrix} \tag{13}$$

$$\begin{Bmatrix} M_x \\ M_y \\ M_{xy} \end{Bmatrix} = \left[\bar{B}\right] \begin{Bmatrix} \varepsilon_x^{(0)} \\ \varepsilon_y^{(0)} \\ \gamma_{xy}^{(0)} \end{Bmatrix} + \left[\bar{D}\right] \begin{Bmatrix} \varepsilon_x^{(1)} \\ \varepsilon_y^{(1)} \\ \gamma_{xy}^{(1)} \end{Bmatrix} \tag{14}$$

$$\begin{Bmatrix} Q_y \\ Q_x \end{Bmatrix} = k_S \left[\bar{K}\right] \begin{Bmatrix} \gamma_{yz}^{(0)} \\ \gamma_{xz}^{(0)} \end{Bmatrix} \tag{15}$$

where the shear correction factor $k_S = 5/6$. The plate stiffness coefficients $(\bar{A}_{ij}, \bar{B}_{ij}, \bar{D}_{ij})$ and $\bar{K}_{ij}$ are calculated by

$$(\bar{A}_{ij}, \bar{B}_{ij}, \bar{D}_{ij}) = \sum_{k=1}^{N_L} \int_{Z_k}^{Z_{k+1}} P_{ij}^{(k)} (1, Z, Z^2) \mathrm{d}Z, \quad (i, j = 1,2,3) \tag{16}$$

$$\bar{K}_{ij} = \sum_{k=1}^{N_L} \int_{Z_k}^{Z_{k+1}} Q_{ij}^{(k)} \mathrm{d}Z, \quad (i, j = 1,2) \tag{17}$$

in which

$$\begin{gathered} P_{11}^{(k)} = P_{22}^{(k)} = \frac{E_C^{(k)}}{1-\nu_C^2}, \quad P_{12}^{(k)} = P_{21}^{(k)} = \frac{\nu_C E_C^{(k)}}{1-\nu_C^2}, \\ P_{33}^{(k)} = Q_{11}^{(k)} = Q_{22}^{(k)} = \frac{E_C^{(k)}}{2(1+\nu_C)}, \quad P_{13}^{(k)} = P_{31}^{(k)} = P_{23}^{(k)} = P_{32}^{(k)} = Q_{12}^{(k)} = Q_{21}^{(k)} = 0 \end{gathered} \tag{18}$$

Strain-displacement relations are defined as

$$\begin{Bmatrix} \varepsilon_x^{(0)} \\ \varepsilon_y^{(0)} \\ \gamma_{xy}^{(0)} \\ \gamma_{yz}^{(0)} \\ \gamma_{xz}^{(0)} \end{Bmatrix} = \begin{Bmatrix} \dfrac{\partial U}{\partial X} \\ \dfrac{\partial V}{\partial Y} \\ \dfrac{\partial U}{\partial Y} + \dfrac{\partial V}{\partial X} \\ \dfrac{\partial W}{\partial Y} + \Psi_y \\ \dfrac{\partial W}{\partial X} + \Psi_x \end{Bmatrix}, \quad \begin{Bmatrix} \varepsilon_x^{(1)} \\ \varepsilon_y^{(1)} \\ \gamma_{xy}^{(1)} \\ \gamma_{yz}^{(1)} \\ \gamma_{xz}^{(1)} \end{Bmatrix} = \begin{Bmatrix} \dfrac{\partial \Psi_x}{\partial X} \\ \dfrac{\partial \Psi_y}{\partial Y} \\ \dfrac{\partial \Psi_x}{\partial Y} + \dfrac{\partial \Psi_y}{\partial X} \\ 0 \\ 0 \end{Bmatrix} \tag{19}$$

Substituting Eqs. (13)-(15) and (19) into Eqs. (8)-(12) and introducing the following dimensionless parameters

$$\begin{gathered} x=\frac{X}{a},\quad y=\frac{Y}{b},\quad u=\frac{U}{h},\quad v=\frac{V}{h},\quad w=\frac{W}{h},\quad \phi_x=\Psi_x,\\ \phi_y=\Psi_y,\quad \alpha=\frac{h}{a},\quad \beta=\frac{a}{b},\quad A_{ij}=\frac{\bar{A}_{ij}}{E_{\mathrm{M}}a},\quad B_{ij}=\frac{\bar{B}_{ij}}{E_{\mathrm{M}}a^2},\quad D_{ij}=\frac{\bar{D}_{ij}}{E_{\mathrm{M}}a^3},\\ K_{ij}=\frac{\bar{K}_{ij}}{E_{\mathrm{M}}a},\quad N_x^0=\frac{\bar{N}_x^0}{E_{\mathrm{M}}b},\quad N_{xy}^0=\frac{\bar{N}_{xy}^0}{E_{\mathrm{M}}b},\quad N_y^0=\frac{\bar{N}_y^0}{E_{\mathrm{M}}b},\quad f=\frac{F}{E_{\mathrm{M}}} \end{gathered} \tag{20}$$

the governing equations can be derived in terms of dimensionless displacement components (u,v,w,ϕ_x,ϕ_y) as

$$\begin{aligned} &\alpha A_{11}\frac{\partial^2 u}{\partial x^2}+\alpha\beta^2 A_{33}\frac{\partial^2 u}{\partial y^2}+\alpha\beta\left(A_{12}+A_{33}\right)\frac{\partial^2 v}{\partial x\partial y}+B_{11}\frac{\partial^2\phi_x}{\partial x^2}\\ &+\beta^2 B_{33}\frac{\partial^2\phi_x}{\partial y^2}+\beta\left(B_{12}+B_{33}\right)\frac{\partial^2\phi_y}{\partial x\partial y}=0 \end{aligned} \tag{21}$$

$$\begin{aligned} &\alpha\beta\left(A_{12}+A_{33}\right)\frac{\partial^2 u}{\partial x\partial y}+\alpha A_{33}\frac{\partial^2 v}{\partial x^2}+\alpha\beta^2 A_{22}\frac{\partial^2 v}{\partial y^2}+\beta\left(B_{12}+B_{33}\right)\frac{\partial^2\phi_x}{\partial x\partial y}\\ &+B_{33}\frac{\partial^2\phi_y}{\partial x^2}+\beta^2 B_{22}\frac{\partial^2\phi_y}{\partial y^2}=0 \end{aligned} \tag{22}$$

$$\begin{aligned} &k_{\mathrm{S}}K_{22}\left(\alpha\frac{\partial^2 w}{\partial x^2}+\frac{\partial\phi_x}{\partial x}\right)+\beta k_{\mathrm{S}}K_{11}\left(\alpha\beta\frac{\partial^2 w}{\partial y^2}+\frac{\partial\phi_y}{\partial y}\right)+\frac{\alpha}{\beta}N_x^0\frac{\partial^2 w}{\partial x^2}+2\alpha N_{xy}^0\frac{\partial^2 w}{\partial x\partial y}\\ &+\alpha\beta N_y^0\frac{\partial^2 w}{\partial y^2}+f=0 \end{aligned} \tag{23}$$

$$\begin{aligned} &\alpha B_{11}\frac{\partial^2 u}{\partial x^2}+\alpha\beta^2 B_{33}\frac{\partial^2 u}{\partial y^2}+\alpha\beta\left(B_{12}+B_{33}\right)\frac{\partial^2 v}{\partial x\partial y}+D_{11}\frac{\partial^2\phi_x}{\partial x^2}+\beta^2 D_{33}\frac{\partial^2\phi_x}{\partial y^2}\\ &+\beta\left(D_{12}+D_{33}\right)\frac{\partial^2\phi_y}{\partial x\partial y}-k_{\mathrm{S}}K_{22}\left(\alpha\frac{\partial w}{\partial x}+\phi_x\right)=0 \end{aligned} \tag{24}$$

$$\begin{aligned} &\alpha\beta\left(B_{12}+B_{33}\right)\frac{\partial^2 u}{\partial x\partial y}+\alpha B_{33}\frac{\partial^2 v}{\partial x^2}+\alpha\beta^2 B_{22}\frac{\partial^2 v}{\partial y^2}+\beta\left(D_{12}+D_{33}\right)\frac{\partial^2\phi_x}{\partial x\partial y}+D_{33}\frac{\partial^2\phi_y}{\partial x^2}\\ &+\beta^2 D_{22}\frac{\partial^2\phi_y}{\partial y^2}-k_{\mathrm{S}}K_{11}\left(\alpha\beta\frac{\partial w}{\partial y}+\phi_y\right)=0 \end{aligned} \tag{25}$$

3. Solution technique

Analytical solution of the above governing differential equations can be obtained by employing Navier solution technique for the nanocomposite plate simply supported at all edges whose boundary conditions require:

$$\begin{aligned} v = w = \phi_y = H_x = M_x = 0 \quad \text{at} \, x = 0,1 \\ u = w = \phi_x = H_y = M_y = 0 \quad \text{at} \, y = 0,1 \end{aligned} \tag{26}$$

The dimensionless displacement functions that satisfy these boundary conditions take the form of the following double trigonometric series

$$u(x,y) = \sum_{r=1}^{R}\sum_{s=1}^{S} U_{rs} \cos r\pi x \sin s\pi y \tag{27}$$

$$v(x,y) = \sum_{r=1}^{R}\sum_{s=1}^{S} V_{rs} \sin r\pi x \cos s\pi y \tag{28}$$

$$w(x,y) = \sum_{r=1}^{R}\sum_{s=1}^{S} W_{rs} \sin r\pi x \sin s\pi y \tag{29}$$

$$\phi_x(x,y) = \sum_{r=1}^{R}\sum_{s=1}^{S} \Phi_{xrs} \cos r\pi x \sin s\pi y \tag{30}$$

$$\phi_y(x,y) = \sum_{r=1}^{R}\sum_{s=1}^{S} \Phi_{yrs} \sin r\pi x \cos s\pi y \tag{31}$$

where U_{rs}, V_{rs}, W_{rs}, Φ_{xrs}, and Φ_{yrs} are unknown coefficients, and r and s are the numbers of half waves in the X- and Y-directions, respectively.

3.1 Bending analysis

The in-plane compressive loads $\bar{N}_x^0$, $\bar{N}_y^0$ are assumed to be zero in the bending analysis. The dimensionless transverse load is expanded in double trigonometric series as

$$f(x,y) = \sum_{r=1}^{\infty}\sum_{s=1}^{\infty} Q_{rs} \sin r\pi x \sin s\pi y \tag{32}$$

where

$$Q_{rs} = 4\int_0^1\int_0^1 f \sin r\pi x \sin s\pi y \mathrm{d}x\mathrm{d}y \tag{33}$$

Substituting Eqs. (27)-(33) into Eqs. (21)-(25), the algebraic equations for bending problems can be obtained

$$[J]\{\Delta\} = \{Q\} \tag{34}$$

where $[J]$ is the stiffness matrix whose elements are given in Appendix A, $\{\Delta\}$ is the unknown displacement vector, and $\{Q\}$ is the force vector

$$\{\Delta\} = \left\{U_{rs}\ V_{rs}\ W_{rs}\ \Phi_{xrs}\ \Phi_{yrs}\right\}^T, \quad \{Q\} = \left\{0\ 0\ Q_{rs}\ 0\ 0\right\}^T \tag{35}$$

3.2 Buckling analysis

The in-plane compressive loads can be rewritten as $N_x^0 = \gamma_1 N_{\mathrm{cr}}$, $N_y^0 = \gamma_2 N_{\mathrm{cr}}$ where N_{cr} is the dimensionless critical buckling load, γ_1 and γ_2 are the in-plane compressive load ratios. It is evident that $\gamma_1 = -1,\ \gamma_2 = 0$ and $\gamma_1 = 0,\ \gamma_2 = -1$ correspond to uniaxial compression in the *X*- and *Y*-directions, respectively. Neglecting the transverse load $f(x, y)$ and substituting Eqs. (27)-(31) into Eqs. (21)-(25) leads to an eigenvalue equation from which the dimensionless critical buckling load N_{cr} can be obtained

$$\left([J] + N_{\mathrm{cr}}[G]\right)\{\Delta\} = \{0\} \tag{36}$$

where all of the elements in matrix [*G*] are zero, i.e. $G_{ij} = 0$ ($i, j = 1,2,...,5$) except for G_{33} which is $G_{33} = m^2\pi^2\frac{\alpha}{\beta}\gamma_1 + n^2\pi^2\alpha\beta\gamma_2$. The lowest eigenvalue obtained from this equation is taken as the dimensionless critical buckling load.

4. Numerical results and discussion

A detailed parametric study on the bending and buckling behaviors of functionally graded multilayer GPL/polymer plates is conducted in this section, with a particular focus on the effects

of distribution pattern, weight fraction, length-to-thickness and length-to-width ratios of GPL nanofillers. Numerical results are presented in both tabular and graphical forms.

4.1 Static bending

As a typical example, a uniformly distributed transverse load $F(X,Y)=F_0$ is considered herein, for which $Q_{rs}=4\lambda_{rs}f_0/(rs\pi^2)$ and $\lambda_{rs}=1-(-1)^r-(-1)^s+(-1)^{r+s}$, $f_0=F_0/E_{\mathrm{M}}$ in Eq. (33).

As there are no results available in open literature for the bending response of graphene based nanocomposite plates, a simply supported aluminum/alumina (Al/ZrO_2-1) functionally graded square plate is taken as an example to validate the present bending analysis. The material properties are

$$\begin{aligned}&\mathrm{Al}:\ E_1=70\mathrm{GPa},\quad \nu_1=0.3,\\ &(\mathrm{ZrO_2})-1:\ E_2=200\mathrm{GPa},\quad \nu_2=0.3\end{aligned} \tag{37}$$

It is assumed that the top and bottom surfaces of the plate are Al and ZrO_2-1 rich, respectively. Its effective material properties, $P(Z)$, are graded through thickness direction according to a power law in terms of the volume fractions of the constituent materials as [32]

$$P(Z)=P_1+(P_2-P_1)V_2(Z) \tag{38}$$

$$V_2=\left(\frac{1}{2}+\frac{Z}{h}\right)^{\vartheta}\quad(\vartheta\geq 0) \tag{39}$$

where P_1 and P_2 denote the properties of Al and ZrO_2-1, respectively, and ϑ is the volume fraction index. By employing the equivalent homogenous laminated structure approach [33-35], the functionally graded plate is divided into a finite number of isotropic and homogenous layers along the thickness direction and the equivalent effective material property of each layer is defined as the average value of Eq. (38) within the layer as [35]

$$P_{\mathrm{eq}}^{(k)}=\int_{Z_k}^{Z_{k+1}}\frac{P(Z)}{Z_{k+1}-Z_k}\mathrm{d}Z,\quad k=1,2,...,N_{\mathrm{L}} \tag{40}$$

Convergence study is first conducted in Table 1 where the dimensionless central deflection

$w_c = 100W_c E_1 h^3/(12(1-\nu^2)F_0 a^4)$ of the functionally graded plate with varying truncated series terms R, S and the total number of layers N_L are compared. As can be observed, convergent results can be achieved when $R = S = 10$ in the double series solution (27)-(31) and $N_L = 10$. The dimensionless central deflection results are compared with those obtained by using the edge-based smoothed finite element method [36], the MLPG method [37], and the element-free kp-Ritz method [38]. Good agreement is achieved.

Table 1. Dimensionless central deflections of a square Al/ZrO_2-1 functionally graded plate under a uniform load ($\vartheta = 0.5$): Convergence study

	$R=1,\ S=1$	$R=10,\ S=10$	$R=20,\ S=20$
$N_L = 10$	0.2408	0.2319	0.2318
$N_L = 20$	0.2413	0.2323	0.2323
$N_L = 30$	0.2414	0.2324	0.2324

Table 2. Comparison of dimensionless central deflections of a square Al/ZrO_2-1 functionally graded plate under a uniform load ($a/h = 5$; $N_L = 10$; $R = S = 10$)

Method	ϑ			
	0	0.5	1	2
Present	0.1717	0.2319	0.2716	0.3121
Ref. [36]	0.1703	0.2232	0.2522	0.2827
Ref. [37]	0.1671	0.2505	0.2905	0.3280
Ref. [38]	0.1722	0.2403	0.2811	0.3221

In what follows, GPL reinforced polymer composite plates of size $0.45\text{m}\times 0.45\text{m}\times 0.045\text{m}$ is considered. Epoxy is chosen to be the matrix material. The material properties are $\rho_M = 1.2\text{g/cm}^3$ [6], $E_M = 3.0\text{GPa}$, $\nu_M = 0.34$ [39] for epoxy and $\rho_{GPL} = 1.06\text{g/cm}^3$, $E_{GPL} = 1.01\text{TPa}$ [6], and $\nu_{GPL} = 0.186$ for GPLs [40]. Without the loss of generality, N_L is assumed to be an even number and the GPL weight fraction of the kth layer for the four GPL distribution patterns are given as Ref. [30], i.e.,

$$g_{\mathrm{GPL}}^{(k)}=\begin{cases} g_{\mathrm{GPL}}^{*} & \text{UD} \\ 4g_{\mathrm{GPL}}^{*}\left(\dfrac{N_{\mathrm{L}}+1}{2}-\left|k-\dfrac{N_{\mathrm{L}}+1}{2}\right|\right)/(2+N_{\mathrm{L}}) & \text{FG-O} \\ 4g_{\mathrm{GPL}}^{*}\left(\dfrac{1}{2}+\left|k-\dfrac{N_{\mathrm{L}}+1}{2}\right|\right)/(2+N_{\mathrm{L}}) & \text{FG-X} \\ 2kg_{\mathrm{GPL}}^{*}/(N_{\mathrm{L}}+1) & \text{FG-A} \end{cases} \tag{41}$$

in which g_{GPL}^{*} is the total GPL weight fraction. Unless otherwise stated, the dimensions of GPLs are $l_{\mathrm{GPL}}=2.5\mu\mathrm{m}$, $w_{\mathrm{GPL}}=1.5\mu\mathrm{m}$, and $h_{\mathrm{GPL}}=1.5\mathrm{nm}$ [6], and its weight fraction is 1.0%. The uniformly distributed load F_0 is $500k\mathrm{Pa}$ in the bending analysis.

Fig. 3 examines the effect of the total number of layers N_{L} on the percentage deflection ratio $w_{\mathrm{C}}/w_{\mathrm{M}}$ of GPL/epoxy nanocomposite plates with different GPL distribution patterns in which w_{C} and w_{M} denote the central deflections of the plate with and without GPLs, respectively. Results show that an addition of a very small amount of GPL nanofillers can significantly reduce the bending deflections of the plate. For example, by adding only 1.0 w.t.% GPLs, the FG-X plate has a much lower central deflection that is only 17% of that of the pure epoxy plate. Among the four GPL distribution patterns considered, FG-X offers the best reinforcing effect, followed by UD then FG-A and FG-O. As can be expected, the deflection of the plate where GPLs are uniformly dispersed (UD) is not affected by N_{L} due to its homogeneous nature. For all functionally graded nanocomposite plates, the deflection initially increases for both FG-O and FG-A plates but decreases for the FG-X plate as N_{L} increases then remains almost constant when $N_{\mathrm{L}}\geq 10\sim 15$. Hence, $N_{\mathrm{L}}=10$ is used in the following calculations.

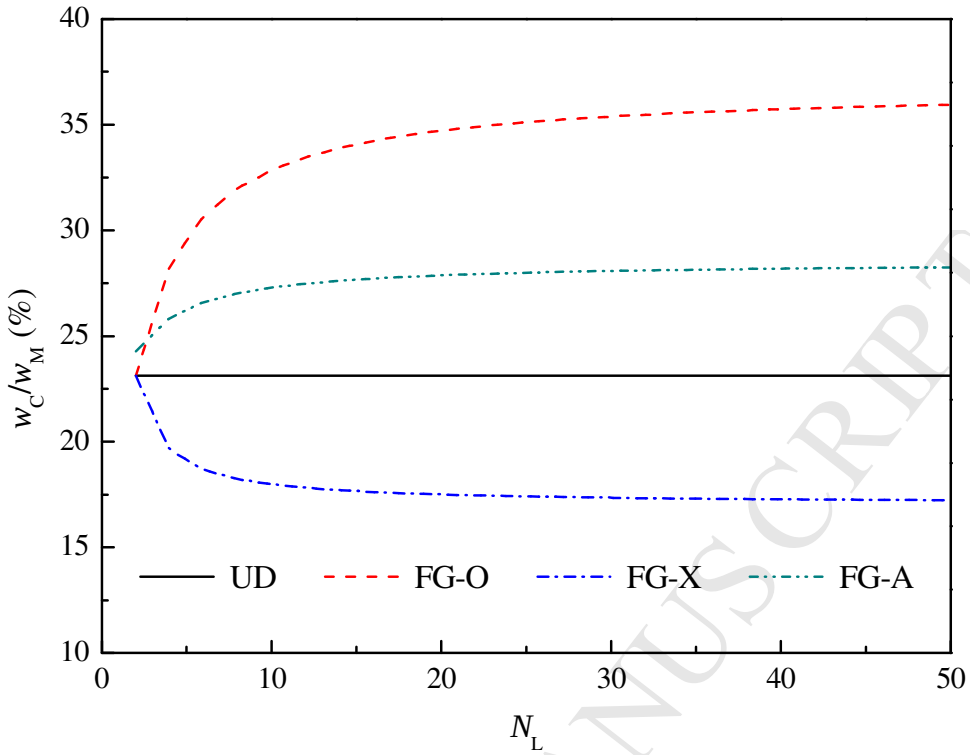

Fig. 3. Effect of total number of layers N_L on deflection ratio w_C / w_M of functionally graded multilayer GPL/epoxy nanocomposite plates.

Fig. 4 demonstrates the effect of GPL weight fraction g^*_{GPL} on the deflection ratio w_C / w_M for GPL/epoxy nanocomposite plates with different distribution patterns. A remarkable drop in central deflection can be observed as GPL weight fraction increases for each distribution pattern. It is also shown that the GPL distribution pattern plays an important role in the static deflections of the plate. By adding the same amount of GPLs, the FG-X distribution pattern gives the smallest deflection, followed by UD, FG-A then FG-O. This is because distributing more GPL nanofillers close to the top and bottom surfaces where the higher normal stress occurs is the more effective way in improving plate stiffness [30].

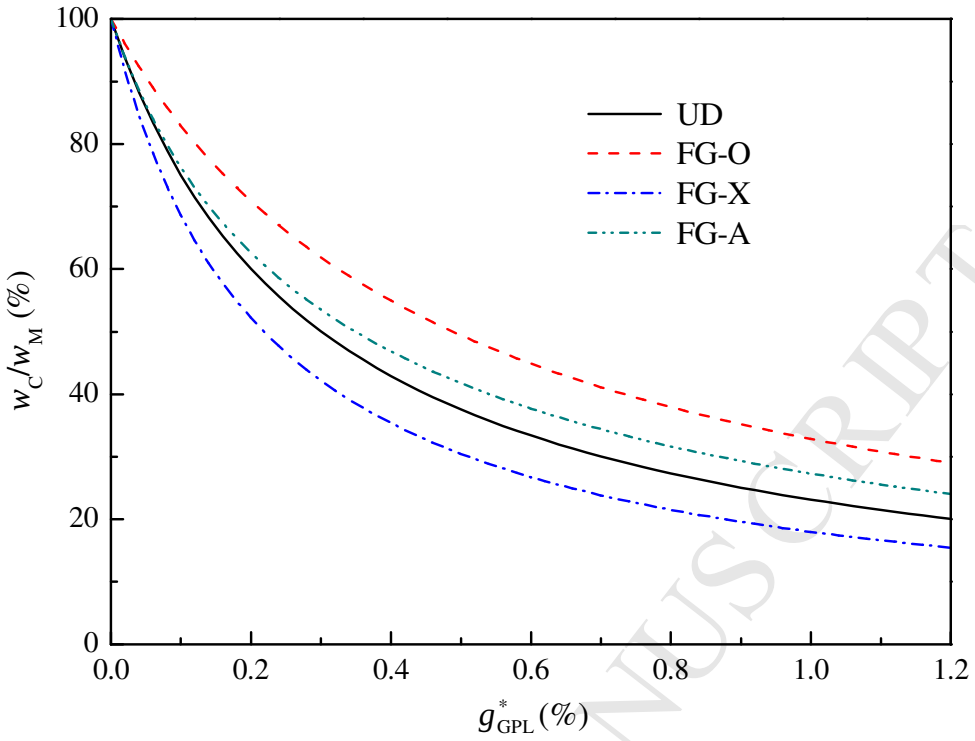

Fig. 4. Effect of GPL weight fraction on w_C / w_M of functionally graded multilayer GPL/epoxy nanocomposite plates

Fig. 5 displays the effects of the geometry and size of GPL nanofillers, in terms of length-to-thickness ratio l_{GPL} / h_{GPL} and length-to-width ratio l_{GPL} / w_{GPL}, on the deflection ratio w_C / w_M for GPL/epoxy nanocomposite plates with different GPL distribution patterns. The average length of GPL nanofillers l_{GPL} is kept constant. The deflection decreases sharply as the l_{GPL} / h_{GPL} ratio increases up to around 2000 then decreases just slightly as l_{GPL} / h_{GPL} further increases. This indicates that GPLs with fewer layers are more effective in reducing the deflection of the plate. In addition, the plate reinforced with square GPLs ($l_{GPL} / w_{GPL} = 1.0$) is seen to have smaller deflection than its counterpart with rectangular GPLs ($l_{GPL} / w_{GPL} = 3.0$), in other words, GPLs with a larger surface area are better reinforcing nanofillers in reducing the deflection of the plate. This is due to the fact that with the same amount of GPLs, a larger contact area between the GPLs and polymer matrix provides better load transfer, which, in turn, leads to higher structural stiffness [30].

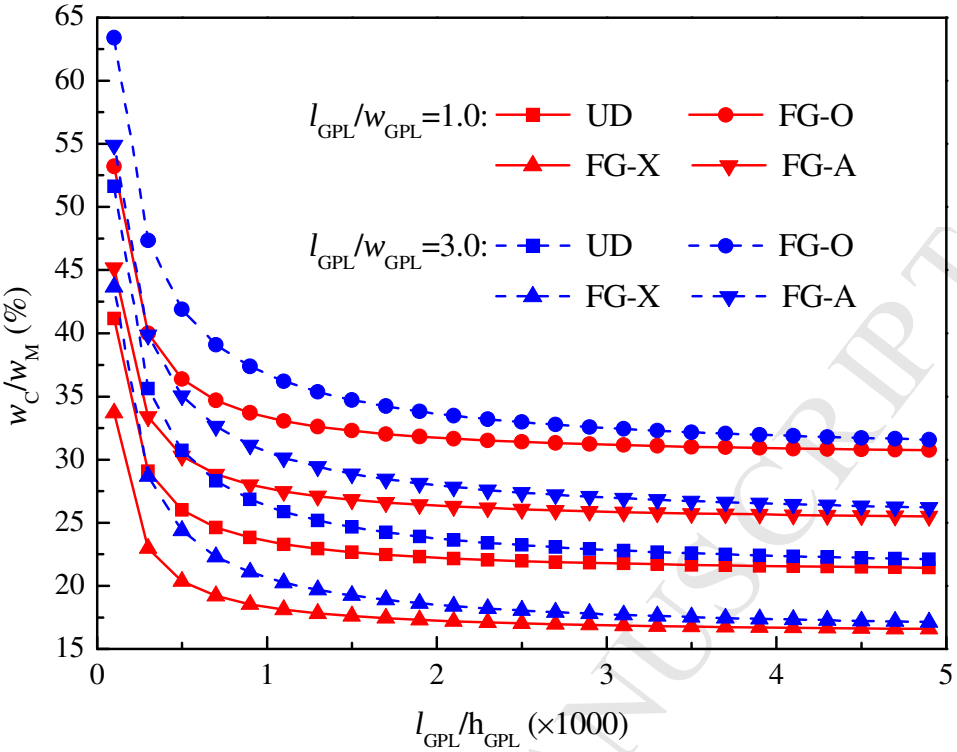

Fig. 5. Effects of GPL geometry and size on w_C / w_M of functionally graded multilayer GPL/epoxy nanocomposite plates.

4.2 Elastic buckling

It is well accepted that due to the bending-stretching coupling effect, even a minimal in-plane force can give rise to deflections and bending moments in an unsymmetrically laminated plate [41]. Hence, bifurcation-type compressive buckling does not occur in a simply supported FG-A plate where GPLs are unsymmetrically dispersed. In this section, elastic buckling analysis will be conducted for UD, FG-O and FG-X plates with symmetrically distributed GPLs only.

Table 3. Comparison of dimensionless critical buckling load ($N_{cr} = \bar{N}_{cr} a^2 / Eh^3$) for simply supported isotropic square plates under uniaxial and equal biaxial compressions

Load type (γ_1, γ_2)	Theory	a/h			
		5	10	20	50
Uniaxial compression $(-1,0)$	Present	2.9498	3.4222	3.5648	3.6000
	Ref. [42]	3.0266	3.4541	3.5821	3.6213
	Ref. [43]	2.9512	3.4224	3.5649	3.6068
Biaxial compression $(-1,-1)$	Present	1.4749	1.7111	1.7824	1.8000
	Ref. [42]	1.5133	1.7271	1.7910	1.8106
	Ref. [43]	1.4756	1.7112	1.7825	1.8034

A simply supported isotropic square plate ($E = 210 \times 10^9$ Pa, $\nu = 0.3$) subjected to a uniaxial compression along the X-direction ($\gamma_1 = -1,\ \gamma_2 = 0$) and equal biaxial compression ($\gamma_1 = -1,\ \gamma_2 = -1$) is considered. The critical buckling loads $N_{cr} = \bar{N}_{cr} a^2 / Eh^3$ are compared in Table 3 with the ones obtained by Sayyad et al. [42] and Reddy [43] for all a/h ratios to validate the present analysis. Again, good agreement is achieved.

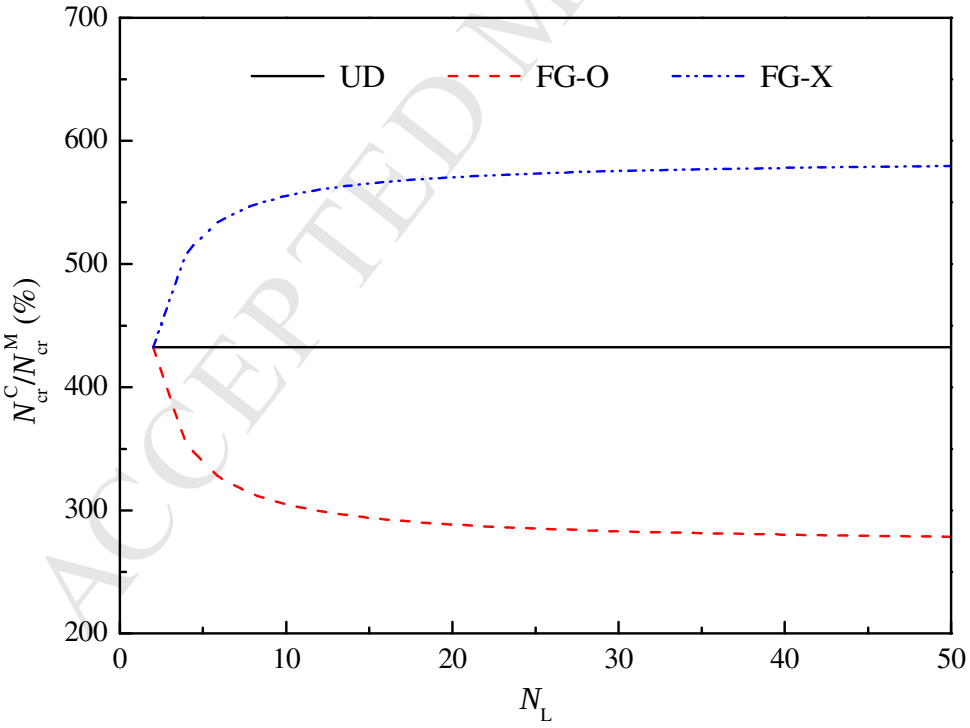

Fig. 6. Effect of total number of layers N_L on N_{cr}^{C} / N_{cr}^{M} for functionally graded multilayer GPL/epoxy nanocomposite plates.

Fig. 6 investigates the effect of the total number of layers N_L on the critical buckling load ratio N_{cr}^{C} / N_{cr}^{M} for the UD, FG-O, FG-X plates, in which N_{cr}^{C} and N_{cr}^{M} stand for critical buckling loads of the plates with and without GPLs, respectively. As the total number of layers increases up to 10~15, the critical buckling load increases for the FG-X plate but becomes lower for the FG-O plate then tends to be constant when $N_L \geq 10 \sim 15$. This is consistent with the results in bending analysis and the observations in Ref. [30], which means that a multilayer structure with a total of 10~15 layers stacked up together can well approximate the ideal functionally graded plate with a continuous and smooth through-thickness gradient in GPL distribution which is extremely difficult and expensive to be fabricated due to the limitation of current manufacturing technology.

Table 4. Dimensionless critical buckling loads of functionally graded multilayer GPL/epoxy plates under uniaxial and equal biaxial compressions

	g^*_{GPL}						
	Pure Epoxy	0.2%	0.4%	0.6%	0.8%	1.0%	1.2%
Uniaxial compression ($\gamma_1 = -1, \gamma_2 = 0$)							
UD	0.0035	0.0058	0.0082	0.0105	0.0128	0.0152	0.0175
		(165.7%)	(234.3%)	(300.0%)	(365.7%)	(434.3%)	(500.0%)
FG-O	0.0035	0.0050	0.0064	0.0078	0.0093	0.0107	0.0121
		(142.9%)	(182.9%)	(222.9%)	(265.7%)	(305.7%)	(345.7%)
FG-X	0.0035	0.0067	0.0099	0.0131	0.0163	0.0195	0.0227
		(191.4%)	(282.9%)	(374.3%)	(465.7%)	(557.1%)	(648.6%)
Biaxial compression ($\gamma_1 = -1, \gamma_2 = -1$)							
UD	0.0018	0.0029	0.0041	0.0053	0.0064	0.0076	0.0088
		(161.1%)	(227.8%)	(294.4%)	(355.6%)	(422.2%)	(488.9%)
FG-O	0.0018	0.0025	0.0032	0.0039	0.0046	0.0053	0.0061
		(138.9%)	(177.8%)	(216.7%)	(255.6%)	(294.4%)	(338.9%)
FG-X	0.0018	0.0034	0.0050	0.0066	0.0082	0.0097	0.0113
		(188.9%)	(277.8%)	(366.7%)	(455.6%)	(538.9%)	(627.8%)

Note: The value in parentheses denotes the percentage critical buckling load ratio N_{cr}^{C} / N_{cr}^{M}.

The effect of GPL weight fraction g^*_{GPL} on the dimensionless buckling loads for UD, FG-O and FG-X plates under uniaxial and equal biaxial compressions is presented in Table 4 where the

value in parentheses denote the percentage critical buckling load ratio N_{cr}^{C}/N_{cr}^{M}. The results of the pristine epoxy plate are also listed for comparison. Apparently, GPL reinforced plates have much bigger critical buckling loads than the pure epoxy plate. For example, an FG-X plate with only 1.0 wt.% GPLs has critical buckling loads that are 557% and 539% of those of the pure epoxy plate under uniaxial and equal biaxial compressions, respectively. This again verifies the significant reinforcing effect of GPL nanofillers even at a low content. It can also be observed that the critical buckling load, which is remarkably improved as GPL weight fraction increases, is the largest for an FG-X plate while the lowest for an FG-O plate. Moreover, the reinforcing effect of GPL nanofillers on the critical buckling load is slightly better under uniaxial compression than under equal biaxial compression.

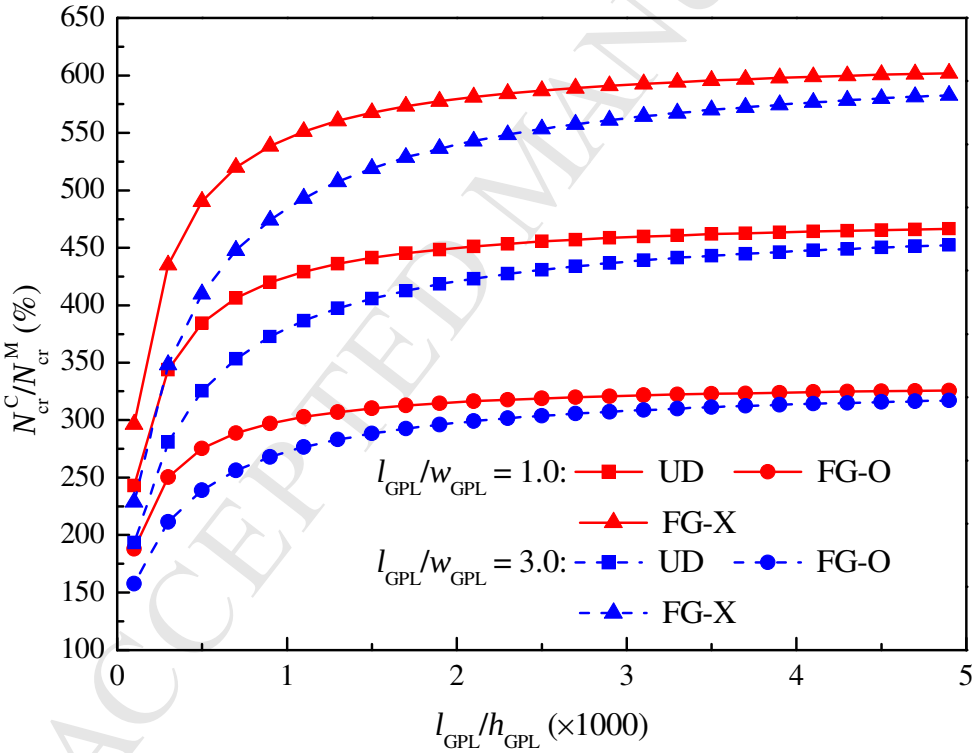

Fig. 7. Effects of GPL length-to-thickness and length-to-width ratios on N_{cr}^{C}/N_{cr}^{M} of functionally graded multilayer GPL/epoxy nanocomposite plates.

Fig. 7 displays the effects of GPL length-to-thickness and length-to-width ratios on the critical buckling load ratio N_{cr}^{C}/N_{cr}^{M} for UD, FG-O, and FG-X plates. It is seen that square shaped GPLs

($l_{GPL}/w_{GPL}=1.0$) outperform the rectangular ones ($l_{GPL}/w_{GPL}=3.0$) in improving the buckling resistance of the plate. The reinforcing effect is further improved by using GPLs with a higher l_{GPL}/h_{GPL} ratio, i.e., with fewer single graphene sheets. However, a further increase in l_{GPL}/h_{GPL} when it goes beyond 2000 results in a slightly higher critical buckling load only.

5. **Conclusions**

The bending and buckling behaviors of functionally graded multilayer GPL/polymer nanocomposite plates have been investigated in this paper within the framework of the first-order shear deformation theory. Navier solution technique is employed to obtain the analytical solutions for the static deflection and critical buckling load of simply supported nanocomposite plates. A parametric study has been conducted. Numerical results reveal that the distribution pattern, weight fraction, geometry, and size of GPL nanofillers have great influences on the bending and buckling characteristics of the plate. An addition of a very small amount of GPLs into the polymer matrix can significantly reduce the bending deflections and increase the critical buckling load. Among the four GPL distribution patterns considered, FG-X is the best way of dispersing GPLs that results in the smallest bending deflections and highest critical buckling load. It is also found that square shaped GPLs with fewer graphene layers are the most favorable reinforcing nanofillers. A multilayer plate consisting of 10~15 layers is an excellent approximation for the desired functionally graded plate with a continuous through-thickness variation in GPL distribution.

Acknowledgements

This work is fully funded by a research grant from the Australian Research Council under Discovery Project scheme (DP160101978). The authors are grateful for the financial support. Dr. Mitao Song is also grateful for the support from the National Natural Science Foundation of China (Grant No. 11302087).

Appendix A

Coefficients shown in Eq. (34) are

$$J_{11}=\alpha\pi^2\left(r^2A_{11}+\beta^2s^2A_{33}\right),\quad J_{12}=\alpha\beta\pi^2rs\left(A_{12}+A_{33}\right),$$

$$J_{13}=0,\quad J_{14}=\pi^2\left(r^2B_{11}+\beta^2s^2B_{33}\right),\quad J_{15}=\beta\pi^2rs\left(B_{12}+B_{33}\right),$$

$$J_{21}=\alpha\beta\pi^2rs\left(A_{12}+A_{33}\right),\quad J_{22}=\alpha\pi^2\left(\beta^2s^2A_{22}+r^2A_{33}\right),$$

$$J_{23}=0,\quad J_{24}=\beta\pi^2rs\left(B_{12}+B_{33}\right),\quad J_{25}=\pi^2\left(\beta^2s^2B_{22}+r^2B_{33}\right),$$

$$J_{31}=0,\quad J_{32}=0,\quad J_{33}=\pi^2\alpha k_S\left(\beta^2s^2K_{11}+r^2K_{22}\right),\quad J_{34}=\pi k_S rK_{22},\quad J_{35}=\pi k_S\beta sK_{11},$$

$$J_{41}=\pi^2\left(r^2B_{11}+\beta^2s^2B_{33}\right),\quad J_{42}=\beta\pi^2rs\left(B_{12}+B_{33}\right),\quad J_{43}=k_S\pi rK_{22},$$

$$J_{44}=\frac{1}{\alpha}\left(\pi^2r^2D_{11}+\pi^2\beta^2s^2D_{33}+k_SK_{22}\right),\quad J_{45}=\frac{\beta}{\alpha}\pi^2rs\left(D_{12}+D_{33}\right),$$

$$J_{51}=\beta\pi^2rs\left(B_{12}+B_{33}\right),\quad J_{52}=\pi^2\left(r^2B_{33}+\beta^2s^2B_{22}\right),\quad J_{53}=k_S\beta\pi sK_{11},$$

$$J_{54}=\frac{\beta}{\alpha}\pi^2rs\left(D_{12}+D_{33}\right),\quad J_{55}=\frac{1}{\alpha}\left(\beta^2\pi^2s^2D_{22}+r^2\pi^2D_{33}+k_SK_{11}\right)$$

References

[1] Novoselov KS, Geim AK, Morozov SV, Jiang D, Zhang Y, Dubonos SV, et al. Electric field effect in atomically thin carbon films. Science 2004; 306:666-669.

[2] Lee C, Wei X, Kysar JW, Hone J. Measurement of the elastic properties and intrinsic strength of monolayer graphene. Science 2008; 321: 385-388.

[3] Balandin AA, Ghosh S, Bao WZ, Calizo I, Teweldebrhan D, Miao F, et al. Superior thermal conductivity of single-layer graphene. Nano Lett 2008; 8: 902-907.

[4] Ghosh S, Bao W, Nika DL, Subrina S, Pokatilov EP, Lau CN, et al. Dimensional crossover of thermal transport in few-layer graphene. Nat Mater 2010; 9: 555-558.

[5] Williams JR, DiCarlo L, Marcus CM. Quantum Hall effect in a gate-controlled pn junction of graphene. Science 2007; 317: 638-641.

[6] Rafiee MA, Rafiee J, Wang Z, Song H, Yu Z-Z, Koratkar N. Enhanced mechanical properties

of nanocomposites at low graphene content. ACS Nano 2009; 3(12): 3884-3890.

[7] Rafiee MA, Rafiee J, Yu Z-Z, Koratkar N. Buckling resistant graphene nanocomposites. Applied Physics Letters 2009; 95(22): 223103.

[8] Rafiee MA, Rafiee J, Srivastava I, Wang Z, Song H, Yu Z-Z, Koratkar N. Fracture and fatigue in graphene nanocomposites. Small 2010; 6(2): 179-183.

[9] Potts JR, Dreyer DR, Bielawski CW, Ruoff RS. Graphene-based polymer nanocomposites. Polymer 2011; 52(1): 5-25.

[10] Montazeri A, Rafii-Tabar H. Multiscale modeling of graphene- and nanotube-based reinforced polymer nanocomposites. Physics Letters A 2011; 375(45): 4034-4040.

[11] Huang X, Qi X, Boey F, Zhang H. Graphene-based composites. Chemical Society Reviews 2012; 41(2): 666-686.

[12] Fang M, Wang K, Lu H, Yang Y, Nutt S. Covalent polymer functionalization of graphene nanosheets and mechanical properties of composites. Journal of Materials Chemistry 2009; 19(38): 7098-7105.

[13] Zhao X, Zhang Q, Chen D, Lu P. Enhanced mechanical properties of graphene-based poly(vinyl alcohol) composites. Macromolecules 2010; 43(5): 2357-2363.

[14] King JA, Klimek DR, Miskioglu I, Odegard GM. Mechanical properties of graphene nanoplatelet/epoxy composites. Journal of Applied Polymer Science 2013; 128(6): 4217-4223.

[15] Wang F, Drzal LT, Qin Y, Huang Z. Mechanical properties and thermal conductivity of graphene nanoplatelet/epoxy composites. Journal of Materials Science 2015; 50(3): 1082-1093.

[16] Ji X-Y, Cao Y-P, Feng X-Q. Micromechanics prediction of the effective elastic moduli of graphene sheet-reinforced polymer nanocomposites. Modelling and Simulation in Materials Science and Engineering 2010; 18(4): 045005.

[17] Rahman R, Haque A. Molecular modeling of crosslinked graphene-epoxy nanocomposites for characterization of elastic constants and interfacial properties. Composites: Part B 2013; 54: 353-364.

[18] Spanos KN, Georgantzinos SK, Anifantis NK. Mechanical properties of graphene

nanocomposites: A multiscale finite element prediction. Composite Structures 2015; 132: 536-544.

[19] Shen H-S. Nonlinear bending of functionally graded carbon nanotube-reinforced composite plates in thermal environments. Composite Structures 2009; 91(1): 9-19.

[20] Shen H-S. Thermal buckling and postbuckling behavior of functionally graded carbon nanotube-reinforced composite cylindrical shells. Composites: Part B 2012; 43(3): 1030-1038.

[21] Tagrara SH, Benachour A, Bouiadjra MB, Tounsi A. On bending, buckling and vibration responses of functionally graded carbon nanotube-reinforced composite beams. Steel and Composite Structures 2015; 19(5): 1259-1277.

[22] Zhang LW, Lei ZX, Liew KM. Free vibration analysis of functionally graded carbon nanotube-reinforced composite triangular plates using the FSDT and element-free IMLS-Ritz method. Composite Structures 2015; 120: 189-199.

[23] Ke L-L, Yang J, Kitipornchai S. Nonlinear free vibration of functionally graded carbon nanotube-reinforced composite beams. Composite Structures 2010; 92(3): 676-683.

[24] Abot JL, Song Y. On the mechanical response of carbon nanotube array laminated composite materials. Journal of Reinforced Plastics and Composites 2010; 29(22): 3401-3410.

[25] Ansari R, Shojaei MF, Mohammadi V, Gholami R, Sadeghi F. Nonlinear forced vibration analysis of functionally graded carbon nanotube-reinforced composite Timoshenko beams. Composite Structures 2014; 113: 316-327.

[26] Guo XY, Zhang W. Nonlinear vibrations of a reinforced composite plate with carbon nanotubes. Composite Structures 2016; 135: 96-108.

[27] Chandra Y, Chowdhury R, Scarpa F, Adhikari S, Sienz J, Arnold C, Murmu T, Bould D. Vibration frequency of graphene based composites: A multiscale approach. Materials Science and Engineering B 2012; 177(3): 303-310.

[28] Cranford SW. Buckling induced delamination of graphene composites through hybrid molecular modeling. Applied Physics Letters 2013; 102: 031902.

[29] Rissanou AN, Power AJ, Harmandaris V. Structural and dynamical properties of

polyethylene/graphene nanocomposites through molecular dynamics simulations. Polymers 2015; 7(3): 390-417.

[30] Song MT, Kitipornchai S, Yang J. Free and forced vibrations of functionally graded polymer composite plates reinforced with graphene nanoplatelets. Composite Structures 2017; 159: 579-588.

[31] Reddy JN. Mechanics of laminated composite plates and shells: theory and analysis. CRC Press; 2004.

[32] Reddy JN, Cheng Z-Q. Three-dimensional solutions of smart functionally graded plates. Journal of Applied Mechanics-Transactions of the ASME 2001; 68(2): 234-241.

[33] Ramirez F, Heyliger PR, Pan E. Static analysis of functionally graded elastic anisotropic plates using a discrete layer approach. Composites: Part B 2006; 37(1): 10-20.

[34] Shakeri M, Mirzaeifar R. Static and dynamic analysis of thick functionally graded plates with piezoelectric layers using layerwise finite element model. Mechanics of Advanced Materials and Structures 2009; 16(8): 561-575.

[35] Aksoylar C, Omercikoglu A, Mecitoglu Z, Omurtag MH. Nonlinear transient analysis of FGM and FML plates under blast loads by experimental and mixed FE methods. Composite Structures 2012; 94(2): 731-744.

[36] Nguyen-Xuan H, Tran LV, Nguyen-Thoi T, Vu-Do HC. Analysis of functionally graded plates using an edge-based smoothed finite element method. Composite Structures 2011; 93(11): 3019-3039.

[37] Gilhooley DF, Batra RC, Xiao JR, McCarthy MA, Gillespie JW. Analysis of thick functionally graded plates by using higher-order shear and normal deformable plate theory and MLPG method with radial basis functions. Composite Structures 2007; 80(4): 539-552.

[38] Lee YY, Zhao X, Liew KM. Thermoelastic analysis of functionally graded plates using the element-free kp-Ritz method. Smart Materials and Structures 2009; 18(3): 035007.

[39] Yasmin A, Daniel IM. Mechanical and thermal properties of graphite platelet/epoxy composites. Polymer 2004; 45(24): 8211-8219.

[40] Liu F, Ming P, Li J. Ab initio calculation of ideal strength and phonon instability of graphene under tension. Physical Review B 2007; 76(6): 064120.

[41] Leissa AW. Conditions for laminated plates to remain flat under in-plane loading. Composite Structures 1986; 6(4): 261-270.

[42] Sayyad AS, Ghugal YM. On the buckling of isotropic, transversely isotropic and laminated composite rectangular plates. International Journal of Structural Stability and Dynamics 2014; 14(7): 1450020.

[43] Reddy JN. A simple higher-order theory for laminated composite plates. Journal of Applied Mechanics-Transactions of the ASME 1984; 51(4): 745-752.